

EUV Resolution Enhancement Techniques (RETs) for k_1 0.4 and below

Stephen Hsu^{*a}, Rafael Howell^a, Jianjun Jia^a, Hua-Yu Liu^a, Keith Gronlund^a, Steve Hansen^b,
Jörg Zimmermann^c,

^aASML Brion, 4211 Burton Dr. Santa Clara, CA 95054, USA; ^bASML Technology Development Center, 2650 W. Geronimo Place, Chandler, AZ 85224; ^cCarl Zeiss SMT GmbH, 73446 Oberkochen, Germany

ABSTRACT

Due to the exponential growth of mobile wireless devices, low-power logic chips continue to drive device scaling. To enable sub-10 nm device scaling at an affordable cost, there is a strong need for single exposure advanced lithography. Extreme ultraviolet lithography (EUVL) is one of the most promising candidates to support the design rules for sub-10 nm. The aggressive mobile device design rules continue to push the critical dimension (CD) and pitch and put very stringent demands on the lithography performance such as pattern placement control, image contrast, critical dimension uniformity (CDU), and line width roughness (LWR).

In this paper we report the latest advances in resolution enhancement techniques to address low k_1 challenges in EUV lithography, specifically: minimizing the pattern placement error, enhancing the through-focus contrast, and reducing the impact of stochastic effects. We have developed an innovative source-mask optimization (SMO) method to significantly reduce edge placement errors (EPE) [1] [2]. Aggressive design rules using the state-of-the-art NA of 0.33 of the NXE:3300B and its successor tools can have imaging below $k_1 = 0.4$, which can extend the current process capabilities for single exposure high volume manufacturing (HVM). Burkhardt et al. reported in a previous study that inserting a sub-resolution assist feature (SRAF) within semi-isolated features introduces strong Bossung tilts and best focus shifts, and a general solution for random pitches is not apparent [3]. Kang observed the same issues and proposed to introduce spherical aberrations to correct these effects while having a global impact on the full-chip [4]. In this work we introduce a new methodology to apply SRAFs to improve contrast, reduce best focus shift, and improve process window. Finally, the lower number of photons of EUV and the small feature size brings serious issue of the stochastic effect that causes the line-edge-roughness (LER) and local CD uniformity (LCDU). Source power, photoresist, mask bias, and feature size all impact the stochastic effects that can result in large LER for low- k_1 patterning. We incorporate an empirical LER model in the SMO NXE frame work to study how the pupil, mask, dose, and target CD can be optimized to reduce stochastic edge placement errors (SEPE). We believe that these advanced EUV RET techniques can support imaging k_1 below 0.4 and extend single exposure for an NA of 0.33, as is used in the NXE:3300B and its successor tools.

Keywords: Extreme ultraviolet lithography (EUVL), critical dimension uniformity (CDU), edge placement errors (EPE), pattern placement error (PPE), line edge roughness (LER). Source mask optimization (SMO), sub-resolution assist features (SRAF), Bossung tilt, best focus shift, stochastic effect

1. INTRODUCTION

The mobile wireless system on a chip (SOC) design continues to drive the miniaturization of semiconductor devices and the continued need for advanced lithography. From Rayleigh's resolution equation, (equation 1), the resolution can be improved in three key ways: decreasing the wavelength, increasing the numerical aperture (NA), and reducing the k_1 factor.

$$R = \frac{P}{2} = k_1 \frac{\lambda}{NA} \quad (1)$$

EUV lithography uses the wavelength of 13.5 nm which improves the resolution by a factor of 14 compared to Argon fluoride (ArF) lithography. At such short wavelength, most materials in the lithography system have strong absorption, and thus EUV lithography requires fully reflective optics and reticle. The consequence of fully reflective optics is that image formation in an EUV projection system is dramatically different from the image formation in a

* stephen.hsu@asml.com

refractive optical projection system. For a reflective projection system the illumination of the mask is off-axis, with the angle between the chief ray axis and the normal direction of the reticle plane being called the chief-ray-angle-at-object (CRAO) side [6]. The oblique CRAO makes the EUV system non-telecentric on the reticle-side. The NXE:3300B scanner has a CRAO of six degrees. An EUV reticle typically uses Ta-based absorber deposited on a Bragg mirror composed of 40-50 molybdenum/silicon (Mo/Si) reflective multilayer stacks which introduce very strong mask topology effects. From the reticle illumination point of view, there is a range of angles which depends on the NA and illumination of the system, centering around the CRAO impinging on the reticle. For horizontal line-space patterns the thick absorber casts a shadow of the incoming light and this “shadowing effect” depends on the incident angle from the illumination pupil (figure 1).

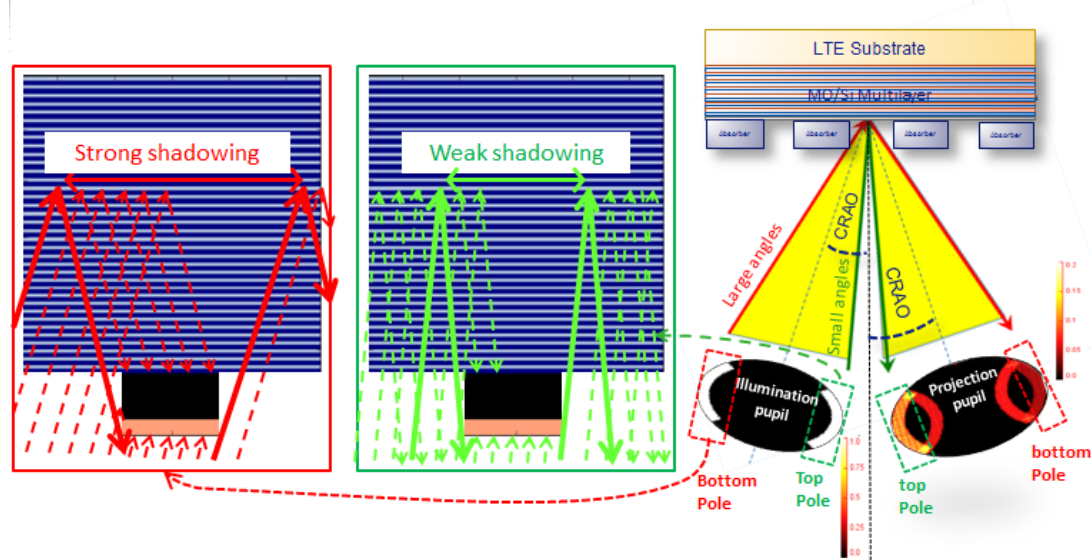


Figure 1: Illustration of the EUV diffraction process. Left: the oblique incident angles impinging on the reticle and strong mask topology and shadow effect. Right: the bottom pole of a dipole that has larger off-axis incidence angles, while the top pole has smaller incidence angles with respect to the normal direction of the reticle. Due to this asymmetry these two poles experience very different imaging conditions that result in diffraction patterns with very strong angular dependency. Two key issues arise from this process: the 0th-order imbalance between the top and bottom pole causes a pattern placement error (PPE) through wafer defocus, and the 0th- and 1st-order imbalance causes contrast lost.

To understand EUV imaging, we must first understand the diffraction pattern of a simple nested line-space grating. Figure 1 shows the EUV diffraction process for a Y-dipole and nested horizontal line-space grating. Due to the oblique incident angles impinging on the reticle and strong mask topology effect, the bottom pole of a dipole has larger off-axis incidence angles, while the top pole has a smaller incidence angles with respect to the normal direction of the reticle. Due to this asymmetry of incident angles, these two poles experience very different imaging conditions. For these line-space patterns the absorber casts a shadow that depends on the thickness of the absorber and the oblique incidence of light. The dependence of this “shadowing effect” on the angle of incident light is illustrated in figure 1: since light from the bottom pole has a larger incident angle, more light is blocked by the absorber and this pole sees a relatively wide effective line width, lower reflectivity whereas light from the top pole has a smaller angle and thus less shadowing and consequently sees a smaller effective line width, higher reflectivity. Simply put, the diffraction pattern has an angular dependency. The right hand side of figure 1 shows the rigorous coupled wave (RCWA) simulation for a 0.33 NA system with six degree CRAO and a 15 nm line-space periodic grating. For comparison purposes, the maximum intensity of the illumination pupil is normalized to one, and the right side of figure 1 shows the projection pupil after light is diffracted from the reticle. Carefully examining the simulated projection pupil, it is clear that the 0th-order of the bottom pole is much more attenuated than the 0th-order of the top pole. This 0th-order imbalance causes a pattern placement error (PPE) through wafer defocus which is termed the telecentricity error [5][6]. In addition, the simulation results also show that the 1st-orders from both the top and bottom poles are much weaker than the corresponding 0th-orders, which leads to contrast loss due to incomplete interference [7][8][9]. With the above analysis, to optimize EUV imaging for k_1 around 0.4, we need to address these issues effectively. Section 2 introduces an innovative pattern placement aware source mask optimization to optimize

the pupil and reduce the pattern placement error (PPE). Section 3 demonstrates the use of assist features to improve the image contrast and reduce the best focus range across different features and improve the overlapped process window. Section 4 demonstrates how to use SMO to improve the image log slope (ILS) and thus reduce the LER. We develop a methodology to show how much an optimized pupil can reduce the LER. Section 5 summarizes the results of these three resolution enhancement techniques.

2. PATTERN PLACEMENT AWARE SOURCE MASK OPTIMIZATION

From the analysis in section 1, it is evident that the 0th-order diffraction imbalance is inherent in the EUV imaging. Conceptually, for a simple Y-dipole, if we want to balance these diffraction orders in the projection pupil we can intentionally introduce a lower intensity in the top pole of the illumination pupil, such that after the diffraction from the reticle the associated diffraction orders in the projection pupil are balanced and thus minimize the pattern placement error (PPE). The PPE is feature size and pitch dependent. Therefore, for a real complex device pattern, optimizing an asymmetric pupil to reduce pattern placement error requires the inclusion of PPE in the optimization framework. Moreover, we need a placement aware process window analysis method to quantify the benefit of such placement aware source mask optimization.

2.1 Improved source mask cost function to reduce pattern placement error

The use of asymmetric pupils to reduce the strong Bossung tilt due to 3D mask topology has been demonstrated [10]. Baseline source and mask co-optimization is driven by a physical cost function: the summation of the L_p norm [1] of edge placement error (EPE) evaluated at all evaluation points through a set of user-specified defocus, delta dose, and mask error conditions. Equation 2 is the formulation of such a cost function:

$$CF = \sum_{pw} \sum_{eval.pts} \|w_{pw,eval} \times EPE(pw, eval. pts)\|^p \quad (2)$$

This cost function works well for a double-sided telecentric projection system. In an EUV system, the reticle side non-telecentricity introduces a 0th-order diffraction imbalance which causes the pattern placement error. For 7 nm node and beyond the pattern placement error can be compounded with the overlay error and erodes the total edge placement budget of 3 to 3.5 nm. Using the simple line-space example in figure 2.1, the L2-norm EPE cost function CF can be written as $CF = epe1^2 + epe2^2$, where epe1 and epe2 are the edge placement of bottom and top edges. However, in this example the cost function cannot differentiate the sign of the EPE from each edge. Figure 2.1 illustrates how the EPEs in two cases have the same magnitude, but the sign of EPE of the upper edge is different than the bottom edge.

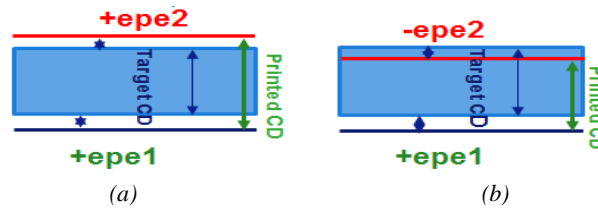


Figure 2.1: EPE of two cases have the same magnitude but opposite signs at top and bottom edge of a line.

By including the sign of the EPE, the CD error can be written as $epe1 + epe2$ and the PPE can be written as $(epe1 - epe2)/2$. In order to minimize pattern placement error due to non-telecentricity in Tachyon SMO NXE, we introduce an innovative cost function by including PPE as part of the cost function: the new cost function becomes $CF = S_{EPE} + S_{PPE}$, where S_{EPE} is the original cost function from equation 2 and S_{PPE} is the pattern placement error through all PW conditions, but only applied at PPE gauge locations. These PPE gauges define where placement errors are taken into account in the optimization.

$$S_{PPE} = W_{PPE} \sum_{pw} \sum_{PPE\ gauge} \|w_{PPE\ gauge} \times PPE(pw, PPE\ gauge)\|^p \quad (3)$$

In the PPE cost function above, W_{PPE} is the weight factor to balance the pattern shift with the CD error, and each PPE gauge can be weighted by $w_{PPE\ gauge}$. This enables RET engineers to minimize the PPE at the critical locations of the design that are sensitive to pattern placement error.

2.2 Placement aware SMO case study

To demonstrate how this pattern placement aware SMO works, a 7 nm logic metal design (see figure 2.2) with minimum CD of 16.8 nm and minimum pitch of 33.6 nm ($k_1 = 0.41$) is used.

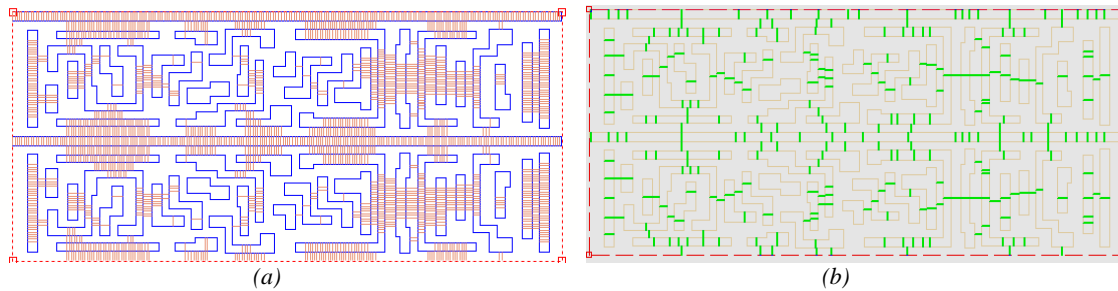


Figure 2.2: (a) L7 logic metal layout with PPE gauges applied. (b) The gauge setup for process window calculation.

Figure 2.2a is the metal design with PPE gauges shown in red. We run three experiments using identical process and setup with different PPE weight (W_{PPE}): 0, 4, and 10. The pupils optimized by SMO without PPE ($W_{PPE} = 0$) and with pattern placement aware SMO with $W_{PPE} = 4$ and $W_{PPE} = 10$ are shown in the top row in figure 2.3. The pupil differences between $W_{PPE} = 0$ and $W_{PPE} = 4$ and between $W_{PPE} = 0$ and $W_{PPE} = 10$ are shown in the bottom row. From the pupil differences we can see that pupil optimized with pattern placement aware SMO shows asymmetry along the y-axis, which corrects the heavy attenuation caused by the strong shadow effect. Furthermore, as the PPE weight increases, the pupil gets more energy at the outer part of the pupil, which alters the 0th-order diffraction pattern amplitude.

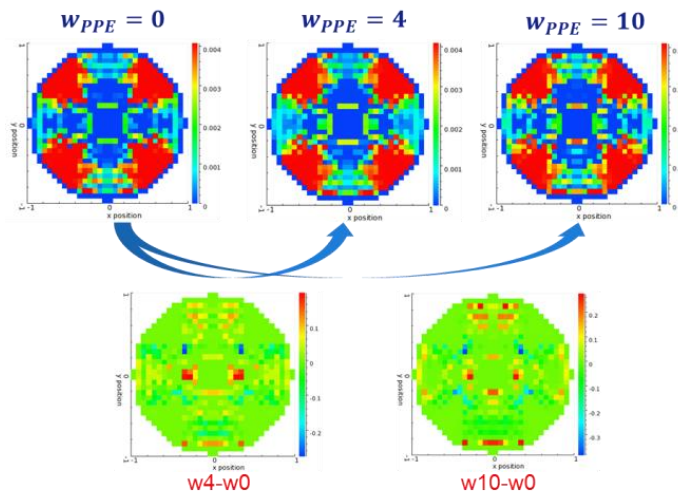


Figure 2.3: Top row: pupils optimized with pattern placement aware SMO using different PPE weight. Bottom row: pupil differences that highlights the pupil energy distribution for different PPE weight.

To quantify the performance of pattern placement aware SMO, we developed a method to calculate the pattern placement aware process window (hereafter PPA PW) which includes the process tolerance for a given pattern placement error. This PPA PW is the overlapped window of the conventional CD-based process window (hereafter ‘CD PW’) and the pattern placement error process window (hereafter ‘PPE PW’). Figure 2.4 shows the CD PW and PPE PW (top row) and the overlapped PPA PW (bottom row) for pattern placement aware SMO using different PPE weights. The top row shows the CD based PW (blue) from all gauges in figure 2.2b with 10% CD tolerance and PPE PW with pattern placement tolerance of 0.4 nm (red). These results clearly show that as the PPE weight increases the PPE PW improves. This leads to significant improvement of the PPA PW since the PPE PW is the overall PW limiter. Figure 2.4b is the exposure defocus (ED) curves for the three PPE experiments: the depth of focus at 10% exposure latitude improves by 46% from 65 nm to 95 nm.

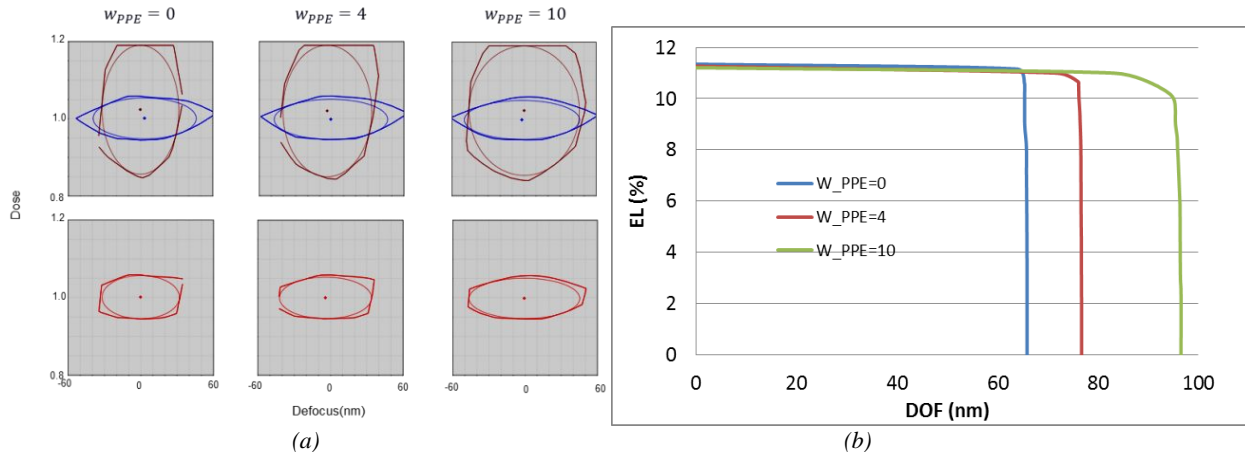


Figure 2.4: (a) Top row: CD-based PW from all gauges in figure 2.2 (blue) and PPE PW with pattern placement tolerance of 0.4 nm (brown). Bottom row: overlapped PW of CD and PPE tolerance. (b) Overlapped ED plot of both CD and PPE PWs.

2.3 Can a symmetric pupil and OPC correct pattern placement error?

As demonstrated in section 2.2, the PPA PW is significantly increased using FlexPupil optimized with pattern placement aware SMO. If we use a standard symmetric pupil, can the pattern placement error be corrected by OPC alone? We carefully selected the standard QUASAR pupil that has the closest pupil shape to the optimized FlexPupil and used the same 7 nm metal design with identical PPE gauges and optimization settings to repeat the experiment. We find that optimizing the mask only cannot improve the PPA PW at the same 0.4 nm PPE tolerance. The PPA PW is 95 nm DOF at 10% EL for the SMO FlexPupil using placement aware SMO with a PPE weight of 10, while for the standard QUASAR with the new cost function only produces a PPA PW of 30 nm DOF at 9% EL.

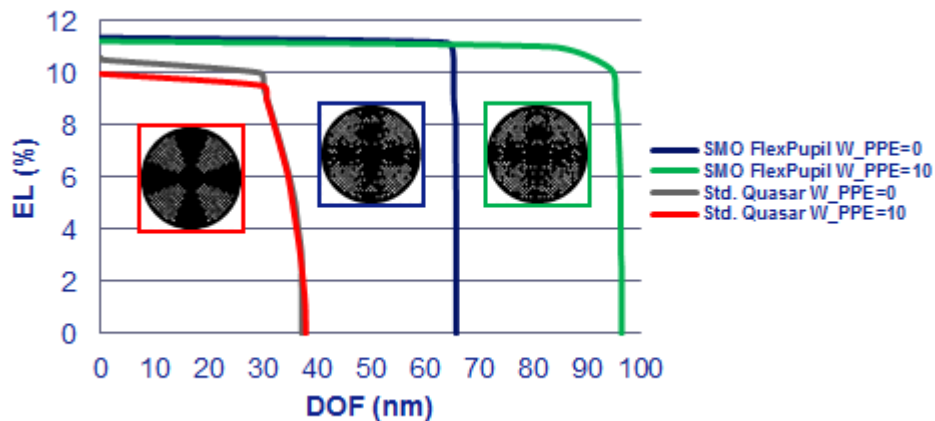


Figure 2.5: Comparison of overlapped ED curves with 0.4 nm PPE tolerance for FlexPupil versus standard QUASAR pupil. The PPA PW is 95 nm DOF at 10% EL for SMO FlexPupil, while for standard QUASAR pupil only produces a PPA PW of 30 nm DOF at 9% EL.

Since the goal of placement aware SMO is to reduce the placement error, we perform more detailed statistical analysis on pattern placement error distributions through defocus, dose, and mask error within the same process window range: defocus [-50 nm, 50 nm] with an increment of 10 nm, dose [0.9, 1.1] with an increment of 0.01 and mask error [-0.25 nm, 0.25 nm] with an increment of 0.25 nm. In total all 292 gauges are measured at 693 process conditions, giving a sample size of 202,356. Figure 2.6 shows the distribution of PPE of all gauges through all PW condition points. The PPE distribution from the standard QUASAR pupil has a wider distribution and larger range

than the SMO FlexPupil. Table 2.1 is a summary of the PPE range and standard deviation. SMO reduces the PPE range by 38%. Even with the PPE differences clearly visible in figure 2.6, we use the two-sample Kolmogorov-Smirnov test [11] to quantify whether the difference of PPE distributions between FlexPupil and standard QUASAR are statistically significant. The null hypothesis is rejected at significance level ($\alpha=0.05$), $D(0.105) > D\alpha(0.004)$, which indicates that the difference of two PPE sample distributions is statistically different. Thus, we conclude that OPC alone cannot improve the pattern placement distribution and the PPE distribution reduction by SMO FlexPupil is statistically significant.

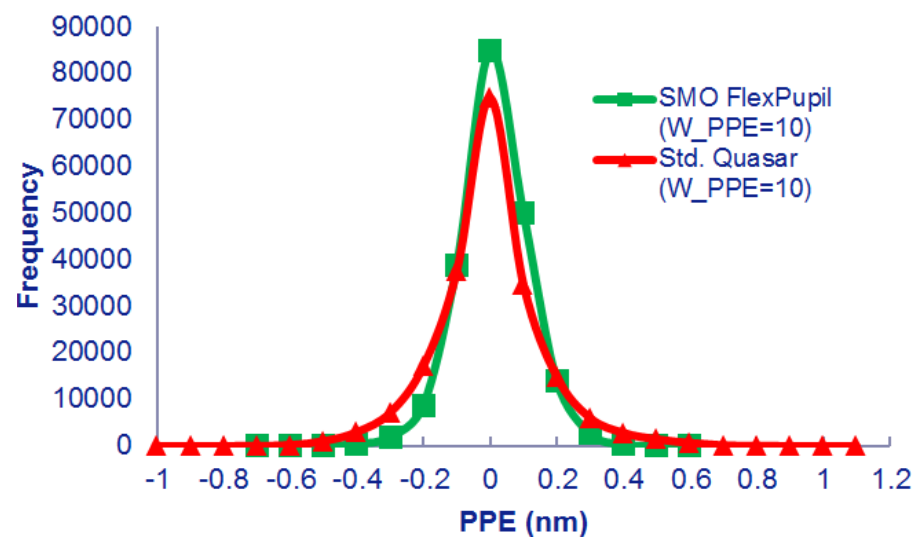


Figure 2.6: PPE distribution through PW conditions for SMO FlexPupil and standard QUASAR using pattern placement aware SMO.

	Negative worst(nm)	Positive worst (nm)	PPE range (nm)	Stdev (nm)
SMO FlexPupil	-0.7	0.6	1.3	0.1
StandardQUASAR	-1.0	1.1	2.1	0.16

Table 2.1: Worst PPE and standard deviation of PPE distributions through PW conditions for SMO FlexPupil and standard QUASAR pupil using pattern placement aware SMO. SMO FlexPupil reduces the PPE by 38%.

3. THE NEED FOR ASSIST FEATURES FOR EUV LITHOGRAPHY

Scattering bars aka Sub-resolution assist features (SRAFs) are the opaque or clear sub-resolution features introduced by Chen as an optical proximity correction technique to improve depth of focus [12][13]. From 180 nm and 130 nm technology nodes, chipmakers have widely adopted SRAFs for KrF and ArF lithography [14]. For 7 nm node low power mobile chip design rules with k_1 values around 0.4, the semi-isolated and isolated features start to limit the overlapped process window. Foundries and integrated device manufacturers have started to conduct experiments on applying SRAFs for EUV and reported their findings and issues. Experimental results from Burkhardt et al. is shown in figure 3.1 (Figure 2 in the reference [3]) from the NXE:3300B scanner for 18 nm trench CD at 72 nm pitch without (left) and with (right) 10 nm wide assist features slot [3]. For the Bossung curves with assist features, strong tilt and best focus shift are clearly observable. To understand this experimental Bossung behavior, we need to understand how such assist features alter the diffraction order amplitudes and phase.

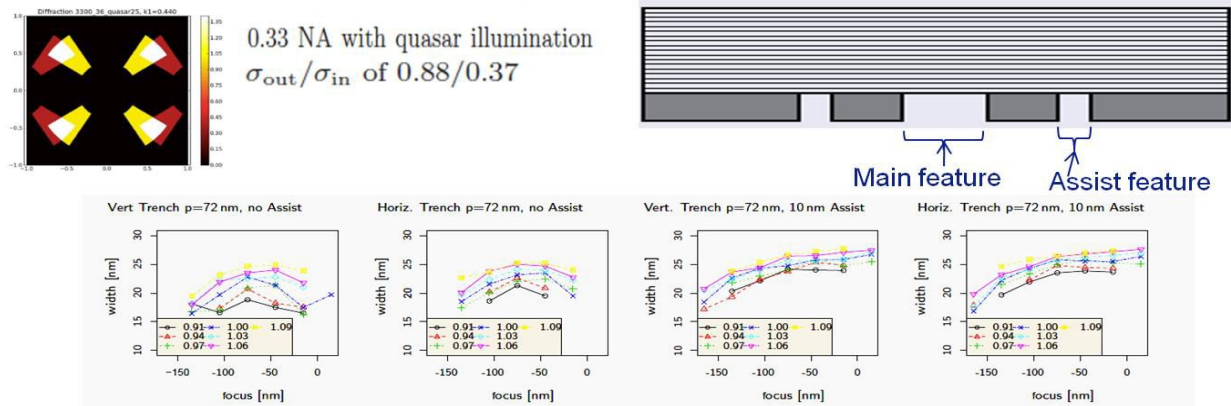


Figure 2. Patterning of vertical and horizontal trenches in resist for 72 nm pitch without (left) and with (right) 10 nm wide assist features. The dose is normalized to best dose for printing equal line and spaces at 36 nm pitch. Best focus is where expected for the non-assisted case, but not determinable in the case for assist features.

Figure 3.1: (a) experimental results from reference [3] show Bossung curves from 18 nm trench, 72 nm pitch without (left) and with (right) 10 nm wide assist features slot. For the Bossung with assist feature, assist feature width = 10 nm, strong Bossung tilt and best focus shift appears.

First, two rigorous RCWA simulations were run using an NA of 0.33 and a Y-dipole with 90° pole angle and inner/outer sigma = 0.52/0.92. The photoresist is 50 nm thick JSR 1915 with 20 nm under coat. These simulations use the same CD and pitch in reference [4] to reproduce the Bossung tilt behavior. The resulting Bossung curves are shown in figure 3.2.

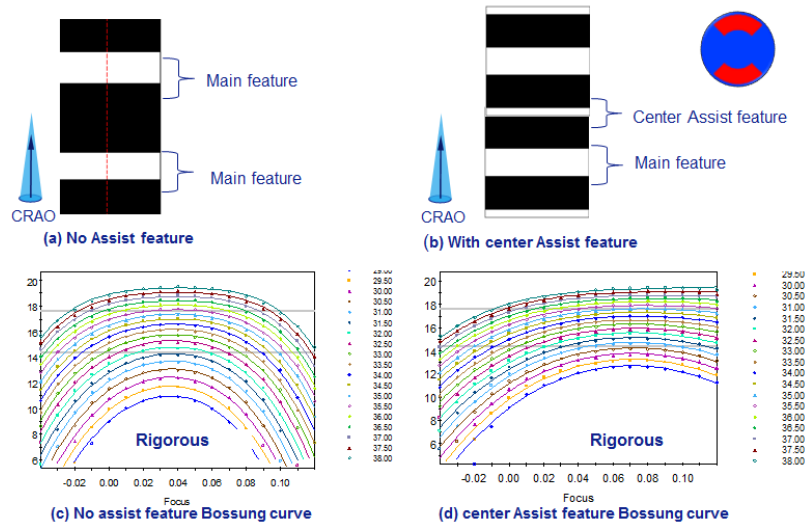


Figure 3.2: horizontal line mask CD = 18.8 nm pitch = 72 nm rigorous simulation Bossung curves with and without a center assist feature. (a) Without an assist feature the Bossung curve is symmetric around the best focus (+ 40 nm). (b) Inserting a 10 nm width center assist feature causes the bossing tilt which is consistent with the experimental result in reference [3].

3.1 Fourier analysis of diffraction pattern with assist features

Figure 3.3 is a cross sectional view of a dark field mask with assist features on each side of the main feature. The width of the main feature is w , the pitch is p , d_1 and d_2 are the assist feature to main feature distances, and s_1 and s_2 are the width of the assist features.

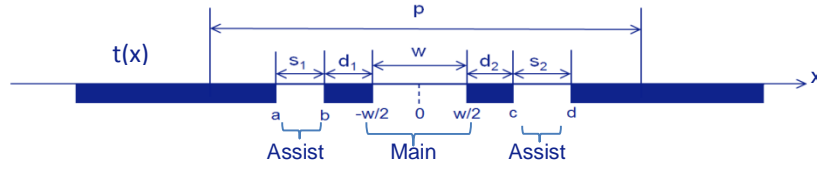


Figure 3.3: cross sectional view of a dark field mask with assist features on each side of the main feature

The electric field of the diffraction pattern $T_m(f_x)$ is:

$$T_m(f_x) = F \{E_i(x) \cdot t_m(x)\} = \int_a^b e^{-2\pi i f_x x} dx + \int_{-w/2}^{w/2} e^{-2\pi i f_x x} dx + \int_c^d e^{-2\pi i f_x x} dx$$

$$= \frac{\sin(\pi w f_x)}{\pi f_x} + \frac{i}{2\pi f_x} (\cos 2\pi f_x b - \cos 2\pi f_x a + i(\sin 2\pi f_x a - \sin 2\pi f_x b)) + \frac{i}{2\pi f_x} (\cos 2\pi f_x d - \cos 2\pi f_x c + i(\sin 2\pi f_x c - \sin 2\pi f_x d)) \quad (4)$$

where $E_i(x)$ is the incident electric field and $t_m(x)$ is the mask field transmittance.

$$\text{Let } s_1 = b - a, \Delta d_1 = b + a = -w - 2d_1 - s_1, s_2 = d - c, \Delta d_2 = d + c = w + 2d_2 + s_2 \quad (5)$$

Equation 4 can be re-written as:

$$T_m(f_x) = \frac{\sin(\pi w f_x)}{\pi f_x} + \frac{1}{\pi f_x} (\cos(\pi f_x \Delta d_1) \sin(\pi f_x s_1) + \cos(\pi f_x \Delta d_2) \sin(\pi f_x s_2) - i(\sin(\pi f_x \Delta d_1) \sin(\pi f_x s_1) + \sin(\pi f_x \Delta d_2) \sin(\pi f_x s_2))) \quad (6)$$

For symmetrically placed assist features, where $d_1 = d_2 = d$ and $s_1 = s_2 = s$, the equations 5 can be simplified into $\Delta d_1 = -\Delta d_2 = \Delta d$. In this symmetric configuration, the imaginary part of equation (6) is zero. As a consequence, inserting symmetric assist features only changes diffraction order amplitude. To investigate how assist features change both the amplitude and the phase, the following four cases are plotted for 50 nm CD at 250 nm pitch: (1) $d_1 \neq d_2, s_1 \neq s_2$, (2) $d_1 \neq d_2, s_1 = s_2$, (3) $d_1 = d_2, s_1 \neq s_2$, (4) $d_1 = d_2, s_1 = s_2$. The first three cases correspond to assist features with different asymmetric configurations, while the fourth case is a symmetric structure used for comparison purpose. Figure 3.4a shows that adding assist features increases the amplitude of higher orders (± 3 and ± 4), which means there is more information about the main features in the diffraction patterns. Adding asymmetric assist features introduces a phase shift between 0th and higher diffraction orders.

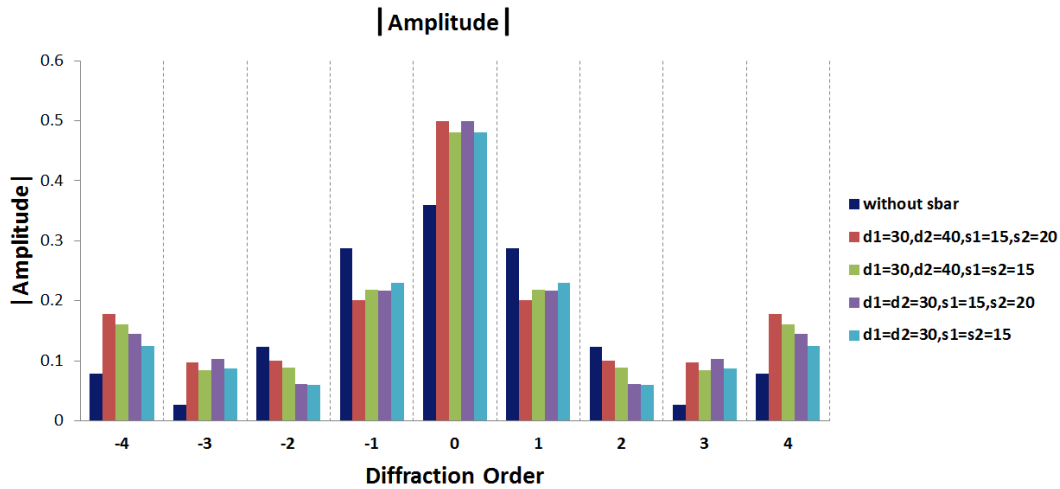


Figure 3.4a

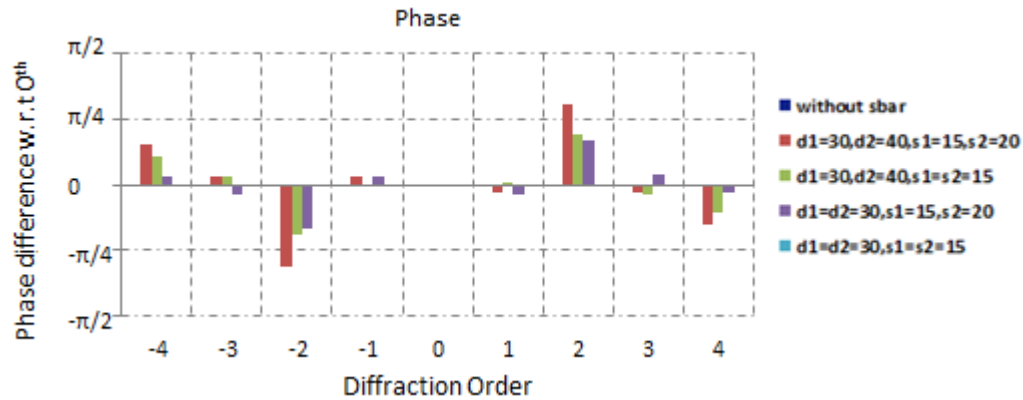


Figure 3.4b

Figure 3.4: The Fourier analysis result of the mask shown in Figure 3.3. Figure 3.4a: inserting symmetric or asymmetric assist features increases the amplitude of higher orders. Figure 3.4b: inserting symmetric assist features only changes diffraction order amplitude and inserting asymmetric assist features introduces a phase shift between the 0th and higher diffraction orders.

With the analysis above, two additional Kirchhoff simulations were run with and without assist features. For the mask with assist features, a 30° phase shift was intentionally introduced between the 0th and higher diffraction orders. Figure 3.5a shows the Bossung plot without center assist feature and figure 3.5b shows the Bossung plot with center assist feature which shows severe Bossung tilt (similar to the rigorous simulation result in figure 3.2d). Figure 3.5c shows the process windows for figure 3.5a and b which clearly show that the process window with the assist feature becomes asymmetric and there is a 20 nm best focus shift with respect to the process window without assist feature. Simulation results in figure 3.5 show that the phase error introduced by the symmetric assist feature is responsible for the Bossung tilt and best focus shift.

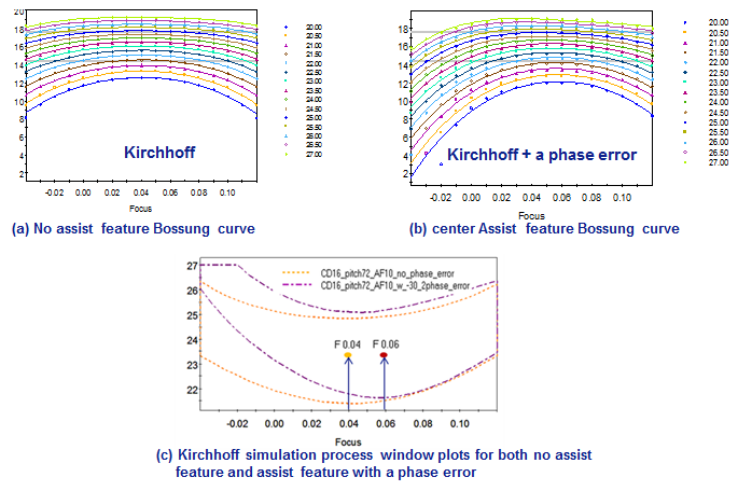


Figure 3.5: Kirchhoff simulation Bossung curve with and without center assist feature. (a) without assist features the Bossung curve is symmetric around the best focus (+ 40 nm). (b) Kirchhoff simulations for the assisted case, a 30° phase error was introduced between 0th and higher order, and the Bossung tilt is clear visible. (c) process window plot comparison for both Kirchhoff simulations, where it is evident that assist features introducing phase errors are the root cause of Bossung tilt and best focus shift.

To demonstrate using the phase effect of asymmetric assist features to “balance” the phase error due to the oblique incident on the mask and thereby reduce the Bossung tilt, a rigorous simulation matrix was setup for different assist feature distances with respect to the top and the bottom of the main feature. The assist feature width is 10 nm for all experiments. For assist feature placement optimization simulations, the design is CD = 16 nm and pitch = 96 nm. An asymmetric pupil was optimized for CD = 16 nm, pitch = 32 nm and 48 nm for these experiments. The simulation

results in figure 3.6 show that the best asymmetric assist feature placement is: top assist feature to main distance is 26 nm and bottom assist feature to main distance is 14 nm.

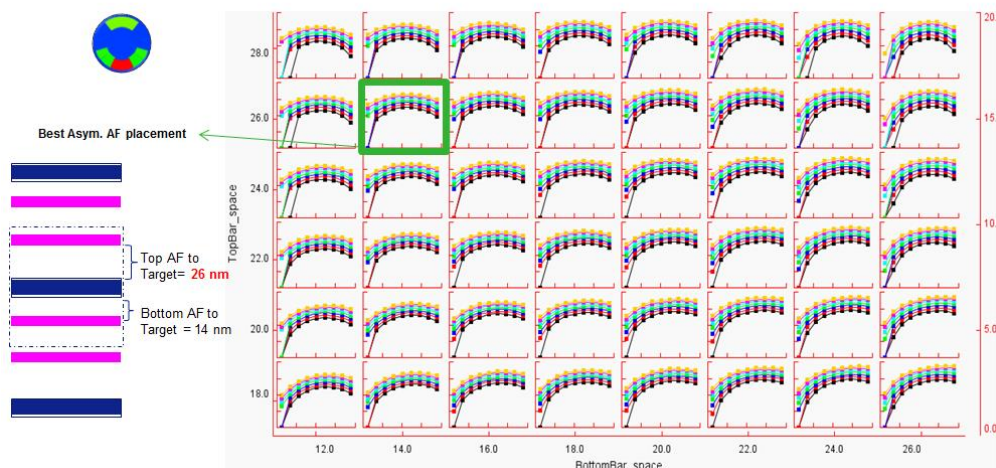


Figure 3.6: Rigorous simulation matrix for different assist feature distance with respect the top and the bottom of the main feature. For assist feature placement optimization simulations the design is CD = 16 nm and pitch = 96 nm. The best asymmetric assist feature placement is: top assist feature to main distance is 26 nm and bottom assist feature to main distance is 14 nm.

3.2 Assist features improve image quality through defocus

One of the key questions for EUV assist features is: do assist features help improve image quality through wafer defocus since the NA is low and k_1 is relatively high compared to the DUV. Additional rigorous RCWA simulations were run to investigate the benefit of assist features for target CD = 16 nm horizontal line at pitch = 96 nm both with and without assist features. In Figure 3.7 the upper row shows the simulated aerial image through wafer defocus with a symmetric Y-dipole. The lower row shows the results from an asymmetric Y-dipole. The dashed line is the intensity threshold. The thin tilted lines show the imbalance of the sidelobes which lead to unwanted assist feature printing. The results show that for both illumination pupils, asymmetric assist features improve the normalized image log slope (NILS) through defocus. In addition, an asymmetric pupil improves the assist feature printability through defocus. These results clearly indicate that for EUV lithography we have to use the technique in section 2 to optimize an asymmetric pupil to control the assist feature printability through wafer defocus.

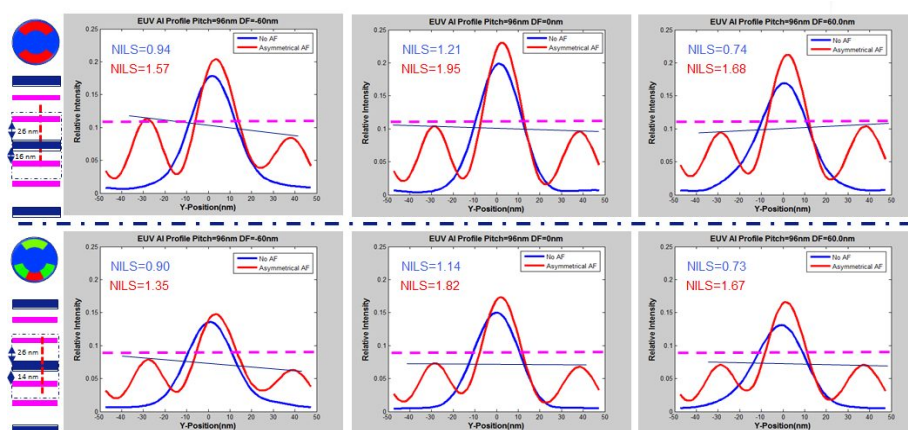


Figure 3.7: Aerial image comparison for a symmetric and asymmetric Y-dipole. For both illumination pupils asymmetric assist features improve the normalized image log slope (NILS) through defocus. In addition, the asymmetric pupil improves the assist feature printability through defocus. The dashed line is the intensity threshold. The thin tilted lines show the imbalance of the sidelobes which lead to unwanted assist feature printing.

3.3 Assist features case study

To study the effect and verify the benefit of asymmetric assist features on device patterns, we consider a 7 nm M2 logic pattern with minimum CD of 15 nm and minimum pitch of 30 nm based on the recent mobile wireless chip design rule (shown in Figure 3.8a). This design also has semi-isolated pitches ranging from 60 nm - 90 nm as well as isolated features. This study is based on this scanner, with NA = 0.33. We first optimized an asymmetric pupil without assist features using Tachyon SMO NXE, the optimized pupil is shown in figure 3.8a. Next, we used the same optimized pupil to optimize the mask with rule-based symmetric and asymmetric assist features. The assist feature width is 10 nm for all experiments. The following lithography metrics are used to assess the imaging performance: overlapped DOF at 10% exposure latitude, PW limiter, and best focus range for all metrology gauges.

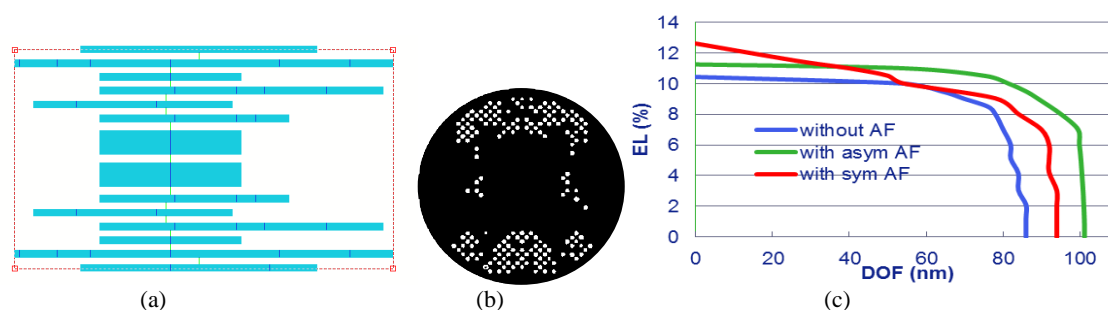


Figure 3.8: (a) 7 nm logic M2 layer with minimum CD 15 nm and pitch 30 nm. This design also has semi-isolated 60 nm and 90 nm pitches; (b) optimized pupil for 7 nm M2 logic pattern in 3.8a without assist feature (c) Exposure Defocus plot of the process window from OPC using the same pupil with and without assist features.

Figure 3.8b plots the overlapped process window comparison of three experiments: layout without assist features, with asymmetric assist features, and with symmetric assist features. Using DOF comparisons at 10% exposure latitude, the case without assist features results in 54 nm, which is increased 52% to 82 nm with asymmetric AF. The symmetric assist features do not improve overlapped PW due to the Bossung tilt. Figure 3.9 shows an example of the Bossung curve of a PW limiter at the same metrology gauge location with symmetric assist features and asymmetric assist features. The gauge location is shown in table 3.1. Figure 3.9 clearly shows that the Bossung tilt is corrected by asymmetric assist features, yet symmetric assist features fail to correct Bossung tilt. Additionally, for both symmetric and asymmetric assist features, the best focus range across all gauges in figure 3.8a is reduced by ~20%. Table 3.1 summarizes the results of these assist feature simulations. From this case study we demonstrate that asymmetric assist features work effectively on a logic design to significantly improve the overlapped process window as expected from the physics developed in section 3.1.

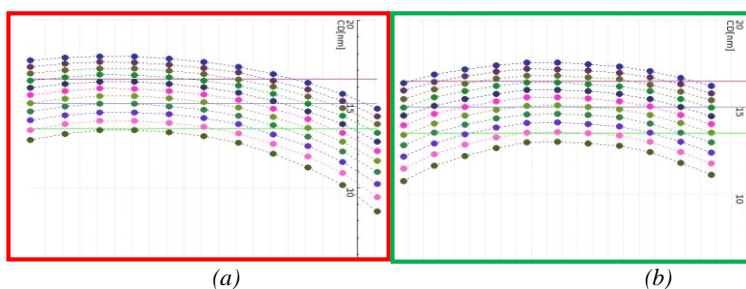


Figure 3.9: Bossung curves of the PW limiter in the simulation with symmetric (left) and asymmetric (right) assist features. The gauge locations are shown in table 3.1 Note that the asymmetric assist features corrected the Bossung tilt.

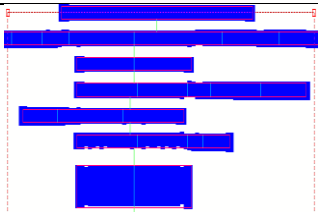

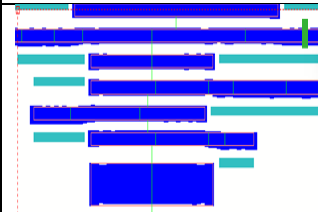
Metric	No assist features	With symmetric assist features (DoF & % gain)	With asymmetric assist features (DoF & % gain)
OPW DoF @ 10%EL	54 nm	54 nm, 0%	82 nm, 52%
Best focus shift range for all gauges, % reduced	47.5 nm (-42 to 5.5)	38.4 nm (-35 to 3.4), 19%	38.7 nm (-30 to 8.7), 19%
L7 metal layer, CD/pitch = 15 / 30 nm Layout without and with assist features			

Table 3.1: Simulation results for L7 metal layer with and without assist features (PW limiter cutlines are marked in the layout).

4. METHOD OF REDUCING LINE EDGE ROUGHNESS

When considering lithography in the molecular scale, the whole process is discrete in nature: light consists of discrete photons and resist reactants are discrete molecules. Continuum models predict the average behavior based on deterministic physics, which is sufficient when there are enough photons and molecules. In EUV lithography, due to very low photo count and very small CD, each lithography process step: exposure, acid generation, and reaction-diffusion, is stochastic and is governed by Poisson statistics [15][16]. Factors that affect line edge roughness (LER) are: statistical local variation of absorbed photons and the affected molecules, resist molecular size, acid diffusion length, dose, and image log slope (ILS) [15]. In this section, we focus on developing a methodology to systematically reduce the LER for a given resist process by studying the effect of illumination efficiency, pupil optimization, dose and CD print bias. Hansen has developed a compact model and a calibration methodology for calculating the stochastic variation in an arbitrary pattern [17]. LER 3-sigma value is characterized by the blurred image ILS dose and image intensity.

$$LER = SEPE = \frac{a}{ILSblur^b} \times (\text{dose} \times \text{blurred image intensity})^c \quad (7)$$

The ILS is calculated from the blurred aerial image obtained by convolution of the aerial image with the empirical one-sigma width that best matches wafer results. The parameters a, b and c can be determined by calibration to wafer data. For a fixed resist process, $SEPE = a/(ILSblur^b)$. Because dose \times blurred image intensity is constant. Current source-mask optimization minimizes the EPE through focus variations, dose variations, and mask errors (figure 4.3a) to minimize the CD variability. The resulting contour through these variations can be plotted as a process variation band (PV band) due to focus, dose and mask error variation. To utilize the SMO framework to directly reduce LER, we incorporated Hansen's LER model as part of the SMO cost function. Since equation (7) is a compact model, we cannot visualize the physical "resist roughness", yet it allows us to simulate and quantify the stochastic effect for a given resist process. Using the similar concept of PV band, we display the LER as a "band due to LER variation", and the line edge roughness can be considered as the localized edge placement error due to stochastic effect. We refer to this effect as the stochastic edge placement error (SEPE) and it can be included as part of the SMO edge placement error optimization frame work.

4.1 EPE and SEPE Optimization

The general cost function form with this stochastic model becomes:

$$CF = \sum(EPE^2 + Wsepe \cdot SEPE^2) \quad (8)$$

where $Wsepe$ is the weighting factor for the SEPE part of the cost function to balance the contribution of the traditional focus, dose, and mask errors with the stochastic contribution to the total cost value during optimization.

Figure 4.1 shows the SMO results for two contact holes with 22 nm CD at 44 nm pitch and 33 nm CD at pitch 60 nm with different SEPE weight. In the NXE:3300B, the illumination pupil consists of discrete pupil spots. The ratio of pupil spots that are switched on to the total available number of pupil channels in the illuminator is defined as the illumination efficiency (IE). For the contact holes in this SEPE study, we set the minimum illumination efficiency = 1 in optimization to constrain the pupil to direct all light to the reticle during the optimization. Figure 4.1a shows that as the SEPE weight increases, the SEPE band decreases at the expense of increasing EPE. In addition, for this case the SEPE is much larger in magnitude than the EPE by approximately a factor of three. A good compromise between SEPE reduction and EPE sacrifice is an SEPE optimization weight of 0.3, where the SEPE band reduces by 18% without a significant trade-off of EPE. Figure 4.1b shows the comparison of the traditional process variation band (PV band) and SEPE band with SEPE weight 0.3 at nominal condition (best focus, best dose), which shows that the 3-sigma SEPE band is larger than the 3-sigma PV band.

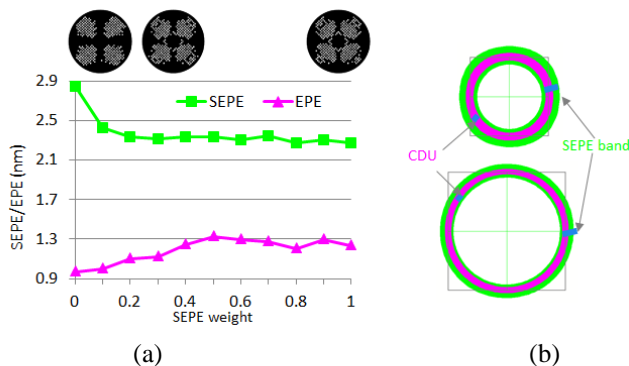


Figure 4.1: SMO results for two contact holes: CD 22 nm at pitch 44 nm and CD 33 nm pitch 60 nm with different SEPE weights.

4.2 SEPE and Illumination Efficiency

It has been experimentally demonstrated that for ArF, the image log slope (ILS) is directly correlated to the line width roughness [18][19]. For EUV, the local CD variation = stochastic dose variation \times dose sensitivity (ILS^{-1}), thus the higher the ILS, the lower the CD variation. Therefore, optimizing the pupil shape specifically to improve the ILS can reduce the LER. We use a logic 7 nm node metal design with minimum CD = 16 at 32 nm pitch (figure 4.2 a) to demonstrate our methodology of minimizing the SEPE using optimal pupil, dose, and print bias. Figure 4.2b shows the optimized NXE:3300B pupil with different illumination efficiencies and the corresponding SEPE value. The general trend is: a lower illumination efficiency gives better ILS and consequently a lower SEPE band. Since the design is mainly vertical lines at 32 nm pitch, the optimized pupil at lower illumination efficiencies has an X-dipole like shape, which allows more complete interference between the 0th- and 1st-order diffraction to give higher ILS.

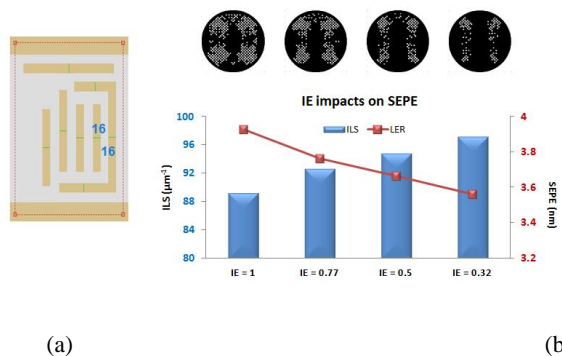


Figure 4.2: (a) a logic 7 nm node metal design with minimum CD = 16 at 32 nm pitch for these SEPE experiments. (b) SMO results with different illumination efficiency. Lower illumination efficiency gives better ILS and lower SEPE band.

4.3 SEPE Reduction through ILS, Dose, and Print Bias Optimization

In the second part of the study, we want to investigate how SEPE can be further reduced with ILS optimization for a given illumination efficiency and fixed resist process [20]. We selected two illumination efficiency settings, IE = 1 and IE = 0.5, the latter value because an NXE:3300B pupil with IE = 0.5 might be realized in future illumination hardware with IE close to 1. The objective of this part of the study is to find out how source mask optimization, with an emphasis on improving NILS by increasing the dose error contribution to the cost function via increasing “dose sensitivity weight” (hereafter delta dose) in optimization conditions, can reduce the SEPE. Further, using this optimized pupil to study how dose (anchor feature mask bias) and print target CD bias can further reduce the SEPE. Figure 4.3b is the result for IE = 1 and 4.3c is the result for IE = 0.5. For both IE settings, the higher the delta dose values the lower the SEPE. Not surprisingly, as the SEPE improved the maximum EPE degraded. For IE = 1, source-mask optimization reduces the SEPE by 13%, and for IE 0.5 the improvement is 9%. IE = 0.5 has less improvement because the IE 0.5 starting point (SEPE = 3.66 nm) is already better than the IE = 1 (SEPE = 3.93 nm).

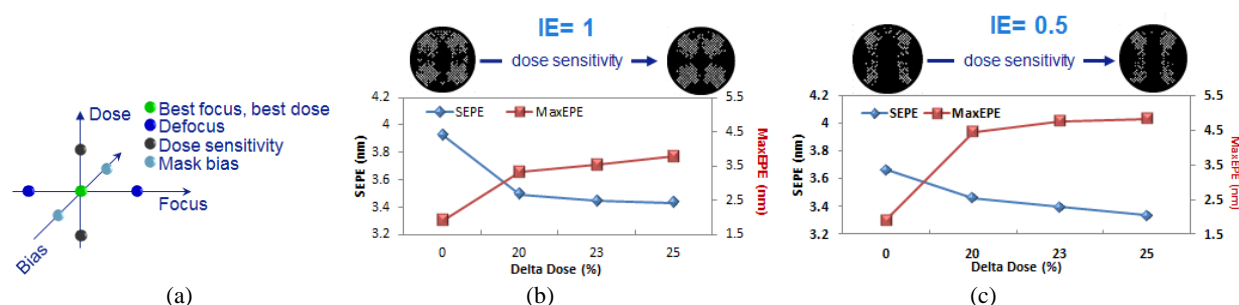


Figure 4.3: used the same design in figure 4.2a for source and mask optimization with emphasis on improving ILS (delta dose). (a) shows the SMO optimization condition, by increasing the delta dose in the optimization improves the ILS [16]. (b) is the result for IE = 1 and (c) is the result for IE = 0.5. For both IE settings the higher the delta dose the lower the SEPE and as the SEPE improved the maximum EPE degraded.

Next, to study the dose and print CD target impact, we used the best IE = 1 and IE = 0.5 pupil to run two sets of simulations by symmetrically varying the dose (anchor mask CD) and global target bias. The dose anchor is CD = 16 nm at 32 nm pitch which equal to dose factor = 1 and the metal target CD is 16 nm which is the global target bias = 0, we set dose factor of this point equals 1 in the experimental matrix. Figure 4.4a is the result for IE = 1 and 4.4b is the result for IE = 0.5. The red circle is the is the baseline run using anchor mask CD (16 nm) and print CD (16nm) (dose factor=1) and the blue circle is the combination of anchor mask CD and print CD that has the lowest SEPE. Both experiments show that higher dose factor (using 12 nm mask to print 16 nm CD) and larger print target CD (print 22 nm trench) improves the SEPE.



Figure 4.4: uses the same design in figure 4.2a and selected best pupil from IE = 1 and IE = 0.5 to run two sets of simulations by systematically varying dose and print target CD. (a) is the result for IE = 1 and (b) is the result for IE = 0.5. For both IE settings, the results show that higher dose and larger global print target CD bias improve the SEPE.

The SEPE reduction methodology is summarized in figure 4.5: first, select the IE that meets the NILS requirements. Second, co-optimize the source and mask to improve the NILS and consequently reduce the SEPE. Finally, use the best pupil to optimize the best combination of dose and print bias to further reduce SEPE. In the N7 metal case, for IE = 1 the overall SEPE improvement is 17 % and for IE = 0.5, the total improvement is 24%.

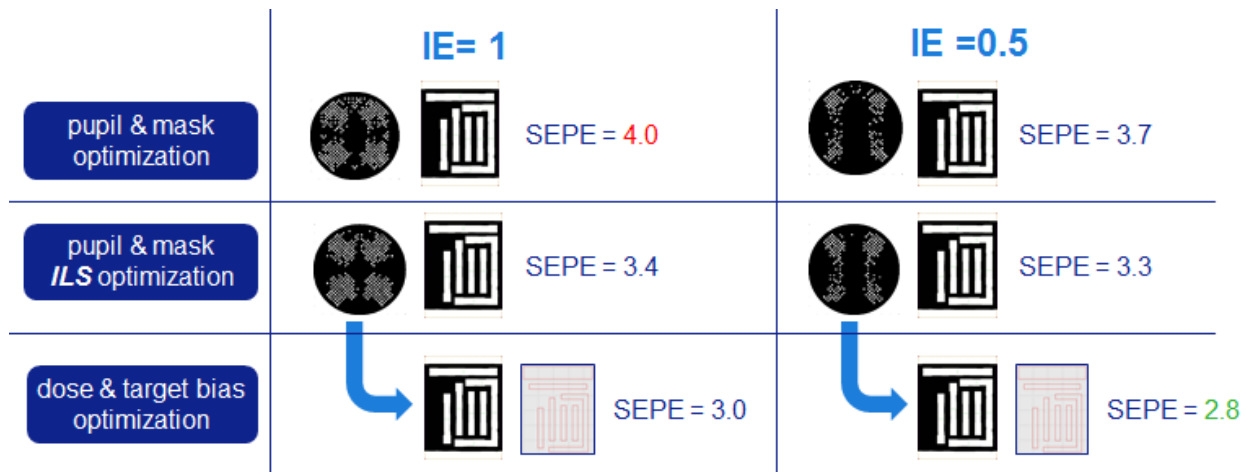


Figure 4.5: Summary of the SEPE reduction flow and results for N7 metal case, for IE = 1 the overall SEPE improvement is 25 % and for IE = 0.5, the overall improvement is 30%.

5. SUMMARY

In this paper, we analyze the fundamental EUV imaging challenges and develop three resolution techniques to address these challenges: first, we formulate an innovative SMO cost function for optimizing an asymmetric pupil to minimize the pattern placement error. Our case study using a 7 nm logic design with newly developed placement aware SMO shows that the PPE distribution reduces by 37% and the DOF at 10% exposure latitude improves from 65 nm to 95 nm (46% improvement). Second, we examine the physics of assist features and get a fundamental understanding of how to properly optimize asymmetric assist features to improve the contrast, reduce the best focus shift between features, and improve the overlapped depth of focus for EUV lithography. We use a $k_1 = 0.39$ 7 nm metal design to demonstrate that by applying correctly-optimized asymmetric assist features, the overlapping DOF improves 52%. Third, we integrate a compact LER model as part of the optimization cost function to reduce the stochastic edge placement error. Furthermore, we demonstrate a methodology on how to systematically reduce the stochastic edge placement error and the results show that for a logic 7 nm node metal case we can reduce the SEPE by 24%. We believe that these new innovative RETs are key enablers for extending EUV lithography to 0.4 k_1 and below.

ACKNOWLEDGMENTS

The authors graciously thank Kurt Wampler, Robert Socha, Jens T. Neumann, Christoph Hennerkes, Frings Liu, Yu Dai, Sam Liu for their assistance, discerning critique and discussion of this work.

REFERENCES

- [1] Stephen Hsu, et al., "An Innovative Source-Mask co-Optimization (SMO) Method for Extending Low k_1 Imaging," Proc. SPIE 7140, 714010-1 (2008).
- [2] Stephen Hsu, et al., "Pattern Placement error aware source mask optimization", US patent application 61955015, March 18, 2014
- [3] Martin Burkhardt et al., "Clear Sub-Resolution Assist Features for EUV," Proc. SPIE. 9048, Extreme Ultraviolet (EUV) Lithography V, 904838. (April 17, 2014) doi: 10.1117/12.2048311

- [4] Hoyoung Kang, Proc. SPIE. 7520, Lithography Asia (2009), 752037. December 03, 2009
- [5] K. Otaki, "Asymmetric properties of the aerial image in extreme ultraviolet lithography", Japan. J. Appl. Phys., Vol 39, 2000
- [6] Joannes Ruoff, , "Impact of mask topography and multilayer stack on high NA imaging of EUV masks," Proc. SPIE 7823,78231N (2010).
- [7] Vicky Philipsen, V. et al., "Impact of mask stack on high-NA EUV imaging," International Symposium on Extreme Ultraviolet Lithography, Brussels (2012).
- [8] Stephen Hsu, et. al "RET integration of CPL technology for Random Logic", SPIE Vol. 5377-46 SPIE 2004
- [9] Jens T. Neumann, et. al "Mask effects for high-NA EUV: impact of NA, chief-ray-angle, and reduction ratio" Proc. SPIE. 8679, Extreme Ultraviolet (EUV) Lithography IV, 867915. (2013)
- [10] Xiaofeng Liu, et. al "EUV source-mask optimization for 7nm node and beyond", Proc. SPIE. 9048, Extreme Ultraviolet (EUV) Lithography V, 90480Q. (2014)
- [11] Conover, W, J. Practical Nonparametric Statistics (1999) 3rd ed, Wiley
- [12] J. F. Chen, et. al, "Practical method for full-chip optical proximity correction" Proc. SPIE. 3051, Optical Microlithography X, 790. (July 07, 1997)
- [13] J. F. Chen, et. al "Optical proximity correction for intermediate-pitch features using sub-resolution scattering bars," J. Vac. Sci. Technol. B, vol. 15, pp 2426-2433, Nov. 1997
- [14] Stephen Hsu, et al, "Lithography Process Optimization for 130nm Poly Gate Mask and the Impact of Mask Error Factor". SPIE Vol. 4344, p 783-796, 2001
- [15] Robert L. Brainard, et al, "Shot noise, LER, and quantum efficiency of EUV photoresists" Proc. SPIE. 5374, Emerging Lithographic Technologies VIII, 74. (May 20, 2004)
- [16] Chris A. Mack, "Line-edge roughness and the ultimate limits of lithography Proc. SPIE. 7639, Advances in Resist Materials and Processing Technology XXVII, 763931. (March 11, 2010)
- [17] Steve G. Hansen, "Model and calibration methodology for calculating the stochastic variation in an arbitrary pattern." US Patent application 61/938,554
- [18] Stephen Hsu, et al. "Double dipole lithography for 65nm node and beyond: a technology readiness review", PMJ 5446-103, p481-498, 2004
- [19] Timothy B. Michaelson, et al. "The effects of chemical gradients and photoresist composition on lithographically generated line edge roughness" Proc. SPIE. 5753, Advances in Resist Technology and Processing XXII, 368. (May 04, 2005)
- [20] Stephen Hsu, et al. "Source-mask co-optimization: optimize design for imaging and impact of source complexity on lithography performance", Proc. SPIE 7520, Lithography Asia 2009